Relation between microscopic interactions and macroscopic properties in ferroics

Jannis Lehmann[1*], Amadé Bortis[1*], Peter M. Derlet[2,3], Claire Donnelly[3,4,5], Naëmi Leo[3,4,6], Laura J. Heyderman[3,4], Manfred Fiebig[1*]

[1]*Laboratory for Multifunctional Ferroic Materials, Department of Materials, ETH Zurich, 8093 Zurich, Switzerland*
[2]*Condensed Matter Theory Group, Paul Scherrer Institute, 5232 Villigen PSI, Switzerland*
[3]*Laboratory for Mesoscopic Systems, Department of Materials, ETH Zurich, 8093 Zurich, Switzerland*
[4]*Laboratory for Multiscale Materials Experiments, Paul Scherrer Institute, 5232 Villigen PSI, Switzerland*
[5]*Cavendish Laboratory, University of Cambridge, Cambridge CB3, United Kingdom*
[6]*Nanomagnetism Group, CIC nanoGUNE BRTA, 20018 Donostia – San Sebastián, Spain*

The driving force in materials to spontaneously form states with magnetic or electric order is of fundamental importance for basic research and device technology. The macroscopic properties and functionalities of these ferroics depend on the size, distribution and morphology of domains, that is, of regions across which such uniform order is maintained[1]. Typically, extrinsic factors like strain profiles, grain size or annealing procedures control the size and shape of the domains[2–5], whereas intrinsic parameters are often difficult to extract due to the complexity of a processed material. Here, we achieve this separation by building artificial crystals of planar nanomagnets that are coupled by well-defined, tunable, and competing magnetic interactions[6–9]. Aside from analysing the domain configurations, we uncover fundamental intrinsic correlations between the microscopic interactions establishing magnetically compensated order and the macroscopic manifestations of these interactions in basic physical properties. Experiment and simulations reveal how competing interactions can be exploited to control ferroic hallmark properties such as the size and morphology of domains, topological properties of domain walls, or their thermal mobility.

Domain formation is key to the functional properties of ferroics. In ferromagnets, which until now represent the class of ferroics technologically most relevant, domain formation is mainly a result of magnetostatic-energy minimisation[2,10]. Currently, however, compensated types of magnetic order such as antiferromagnetism and ferrotoroidicity are gaining attention with a view to an advanced memory or spintronic technology[11–14]. Due to their zero net magnetisation, domain formation is

no longer a consequence of the demagnetising field, which means that less understood, yet fundamental factors of equal importance come to the fore. While thermodynamics can make general macroscopic predictions about domain formation, it does not reveal the underlying microscopic mechanisms for this formation. Therefore, the link between the microscopic interactions and the macroscopic physical properties remains largely unclear. Unfortunately, extrinsic effects such as the strain distribution, magnetoelastic interactions or annealing protocols[4,5,15] compete with the sought-after intrinsic effects, making the separation of the latter from the former challenging. For the identification and control of the intrinsic coupling mechanisms, a magnetically compensated system with tunable competing microscopic interactions that dominate over the extrinsic contributions is therefore required.

This we accomplish by fabricating artificial two-dimensional arrays of nanomagnets that establish a magnetically compensated ferroic order[16]. The transfer from atomic to sub-micrometre length scales requires the replacement of the quantum-mechanical exchange interaction by the classical magnetic-dipole interaction as the basis for the ferroic order[17–19]. This approach to scaling up yields key advantages such as direct experimental access to the magnetic state, and the possibility to tailor and implement spin-spin interactions with a degree of control that natural materials cannot offer. Such artificial spin systems have already proven their ability to answer general questions about fundamental magnetic properties, including magnetic correlations[20], frustration[21], emergent magnetic monopoles[22,23], thermal fluctuations[24,25], phase transitions[26] and relaxation behaviour[27,28]. Most of these systems are artificial spin ices without macroscopically distinguishable order-parameter-related domain states and parametrised by a single microscopic interaction. The few nanomagnetic systems utilising magnet arrangements with multiple and potentially competing couplings[9,29,30] do not exhibit a ferroic order parameter either. Recent work, however, has shown that the so-called toroidal square array exhibits a magnetically compensated long-range-ordered ground state characterised by the toroidisation as a primary ferroic order parameter (see Methods) and distinct domain states[16].

Here we make use of the toroidal square array comprised of parallel and orthogonal pairs of nanomagnets, with each magnet carrying an in-plane magnetic moment $\mathbf{m}$ along the long axis as shown in Fig. 1a. Due to the anisotropy of the magnetic-dipole coupling, such an arrangement promotes two interactions $J_\perp$ and $J_\parallel$ between orthogonal and parallel nearest neighbours, respectively (see Methods and Fig. 1). These two interactions can be seen as classical magnetic-dipole-based analogues to antisymmetric and symmetric exchange interactions as fundamental ingredients determining the magnetic order in materials.

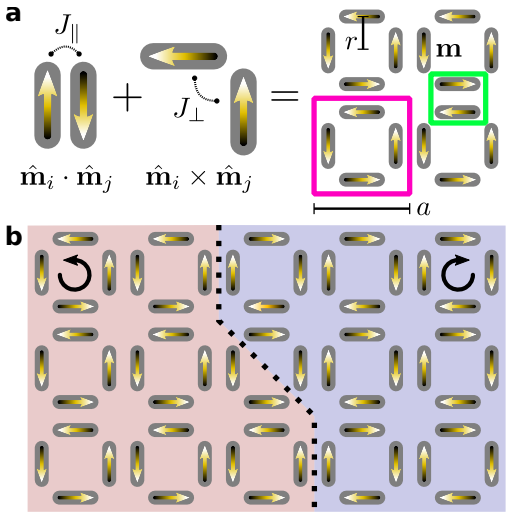

Figure 1: **Model of a ferroic crystal with zero net magnetisation and two competing microscopic interactions. a**, Two-dimensional arrangement of magnetic moments ($\mathbf{m} = |\mathbf{m}|\,\hat{\mathbf{m}}$, yellow arrows), coupled via magnetic-dipole interactions that are classical analogues of antisymmetric ($J_\perp$) and symmetric ($J_\parallel$) exchange interactions. Note that the the coupling constants ($J_\perp, J_\parallel$) are each represented by one of the two geometric units (r, a) parametrising the structure of the system (see Methods). Outlines: Subunits formed by four nanomagnets (octupoles, magenta frame) and two nanomagnets (quadrupoles, green frame) are promoted by $J_\perp$ and $J_\parallel$, respectively. **b**, Ferroic order of the two-dimensional array with domain states that are distinguished by the uniform handedness of the unit cells outlined in magenta in (a): clockwise (blue shading) and counter-clockwise (red shading). A domain wall is indicated by the black dotted line.

A possible periodic arrangement resulting from the combination of $J_\perp$ and $J_\parallel$ is shown in Fig. 1b. It is one of the simplest systems that allows us to study the consequences of the competition between two intrinsic microscopic interactions for the macroscopic properties of a ferroic state with zero net magnetisation. For focusing on the most fundamental consequences, we refrain from adding further ingredients, such as additional magnetic-anisotropy contributions, to our model. The particular spin arrangement in Fig. 1 can be effectively modelled with a Hamiltonian derived from a point-dipole approximation (see Methods), namely

$$\mathcal{H} \;=\; J_\perp \sum_{<i,j>_\perp} \hat{\mathbf{D}}_{ij} \cdot (\hat{\mathbf{m}}_i \times \hat{\mathbf{m}}_j) \;+\; J_\parallel \sum_{<i,j>_\parallel} \hat{\mathbf{m}}_i \cdot \hat{\mathbf{m}}_j \quad , \tag{1}$$

where $\hat{\mathbf{m}}_{i,j}$ are magnetic-moment unit vectors of neighbouring nanomagnets at lattice sites i, j

and $\hat{\mathbf{D}}_{ij}$ is the classical representation of the Dzyaloshinskii-Moriya vector. We can then explore how the relation between $J_\perp$ and $J_\parallel$ in Eqn. (1) controls characteristic macroscopic observables of ferroic order such as the domain size or domain-wall morphology.

First, equilibrium Monte-Carlo simulations are used to calculate the phase diagram in Fig. 2 as a function of $J_\perp/J_\parallel$ using simulated annealing, starting from high temperatures and then decreasing the temperature to well below the ordering temperature T_c of the array. In the upper part of Fig. 2a,b, where $J_\perp \gg J_\parallel$, the dominance of $J_\perp$ promotes the alignment of four magnetic moments, as shown in Fig. 1a, to form a magnetic flux-closure state that mimics the magnetic-field configuration of an octupole. The octupole population density that saturates well above T_c implies that thermal fluctuations of single-nanomagnet dipoles are replaced by fluctuations of four-nanomagnet octupoles. The interaction between octupoles drives the phase transition to long-range order, now defined by the weaker coupling parameter $J_\parallel$. Likewise, in the lower part of Fig. 2a,b, where $J_\perp \ll J_\parallel$, the ordering process is dominated by $J_\parallel$ such that pairs of neighbouring parallel moments (see Fig. 1a) form fluctuating two-nanomagnet quadrupoles above T_c. Their long-range ordering is then driven by the weaker coupling parameter $J_\perp$. In the centre part of Fig. 2, where $J_\perp \approx J_\parallel$, the nanomagnets continue to fluctuate individually as the temperature is reduced to T_c with the phase transition being characterised by a simultaneous increase of octupole and quadrupole density near T_c, see Fig. 2b. Hence, systems with different $J_\perp/J_\parallel$ ratios differ in their short-range order above T_c and thus in their pathways towards long-range order on reducing the temperature. Note that all three pathways lead to the same long-range ordered ground state, so that the macroscopic physical properties of the system are not affected by symmetry changes, but exclusively by the interplay of the two microscopic coupling parameters $J_\perp$ and $J_\parallel$.

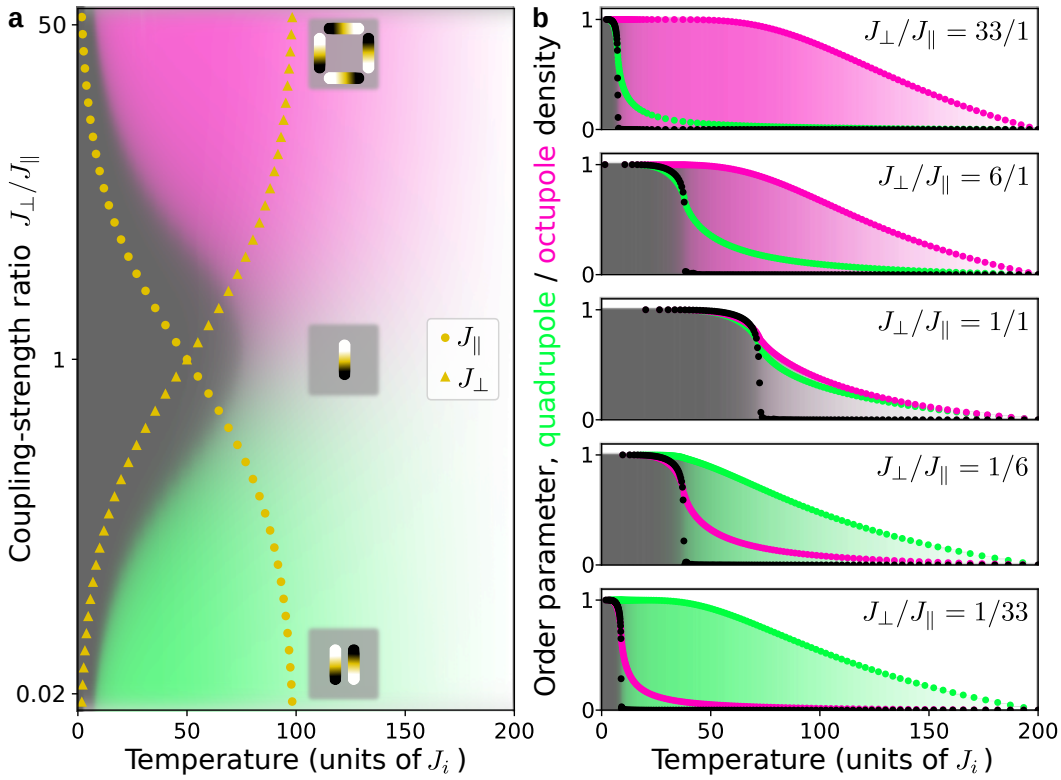

Figure 2: **Phase diagram revealing the correlation between short-range and long-range order. a**, MC-simulated phase diagram of the model Hamiltonian in Eqn. (1) for different coupling-strength ratios $J_\perp/J_\parallel$. The two varying coupling strengths are represented by yellow triangles and circles, respectively. The regions dominated by the octupole- and quadrupole-subunit formation (see text) are shaded magenta and green, respectively. Grey shading indicates the long-range-ordered ground state. **b**, Temperature dependent short- and long-range order for five exemplary choices of $J_\perp/J_\parallel$. The multipole-population densities in (a) and (b) are reflected by the intensity of the colour shading.

To study the impact of the short-range order on the formation of domains, we employ kinetic Monte-Carlo (kMC) simulations and perform a temperature quench from $T \gg T_c$ to $T \ll T_c$. Under identical cooling conditions, we obtain the non-equilibrium multi-domain configurations shown in Fig. 3a for five values of $J_\perp/J_\parallel$ corresponding to the five values shown in Fig. 2b. The domain size reaches a maximum for $J_\perp \approx J_\parallel$ and decreases continuously with an increasing imbalance of $J_\perp$ and $J_\parallel$. While the relationship between the ordering temperature and the domain size might be concluded from a thermodynamics point of view, here we see explicitly how the competition between the exchange coupling constants, an intrinsic microscopic factor, controls the

domain size, which is a macroscopic property of a magnetically compensated ordered state.

We verify this insight experimentally by growing a series of two-dimensional arrays composed of sub-micrometre-sized single-domain ferromagnetic building blocks with the magnetisation pointing along the long axis as schematically shown in Fig. 1 (see Methods). We tune $J_\perp$ and $J_\parallel$ by varying the lateral spacing between the magnets while conserving the size of the four-magnet unit cell (see Fig. 3b). Although the arrays are thermally inactive at room temperature, they are in a superparamagnetic state during growth before their increasing thickness suppresses fluctuations so that the magnetic configuration freezes[31,32]. The resulting domain configurations are imaged by magnetic force microscopy (see Methods).

The agreement between the simulated and the measured domain configurations in Figs. 3a and 3c, in terms of size and morphology, is remarkable. Note that, for $J_\perp \gg J_\parallel$, domain walls align horizontally and vertically between strongly-coupled four-nanomagnet octupoles (left panel in Fig. 3d,e). In a similar way, for $J_\perp \ll J_\parallel$, domain walls run diagonally between strongly-coupled two-nanomagnet quadrupoles (right panel in Fig. 3d,e). For $J_\perp \approx J_\parallel$ (centre panel in Fig. 3d,e), a combination of both wall types is observed. Along with the preferential alignment of a domain wall, the handedness of the magnetisation within a wall can be tuned from equal ($J_\perp \gg J_\parallel$) to opposite ($J_\perp \ll J_\parallel$) with respect to the magnetic handedness of the enclosed domain as shown in Fig. 3d. A particularly interesting case occurs for $J_\perp \approx J_\parallel$, where the direction of magnetisation along the wall alternates due to the competition between the two domain-wall types. Here the walls as such can be regarded as one-dimensional ferromagnetic multi-domain entities with head-to-head or tail-to-tail meeting points of magnetic moments, similar to so-called Bloch points, also described as emergent magnetic charges[22,23,29,33] as indicated in the centre panel of Fig. 3e.

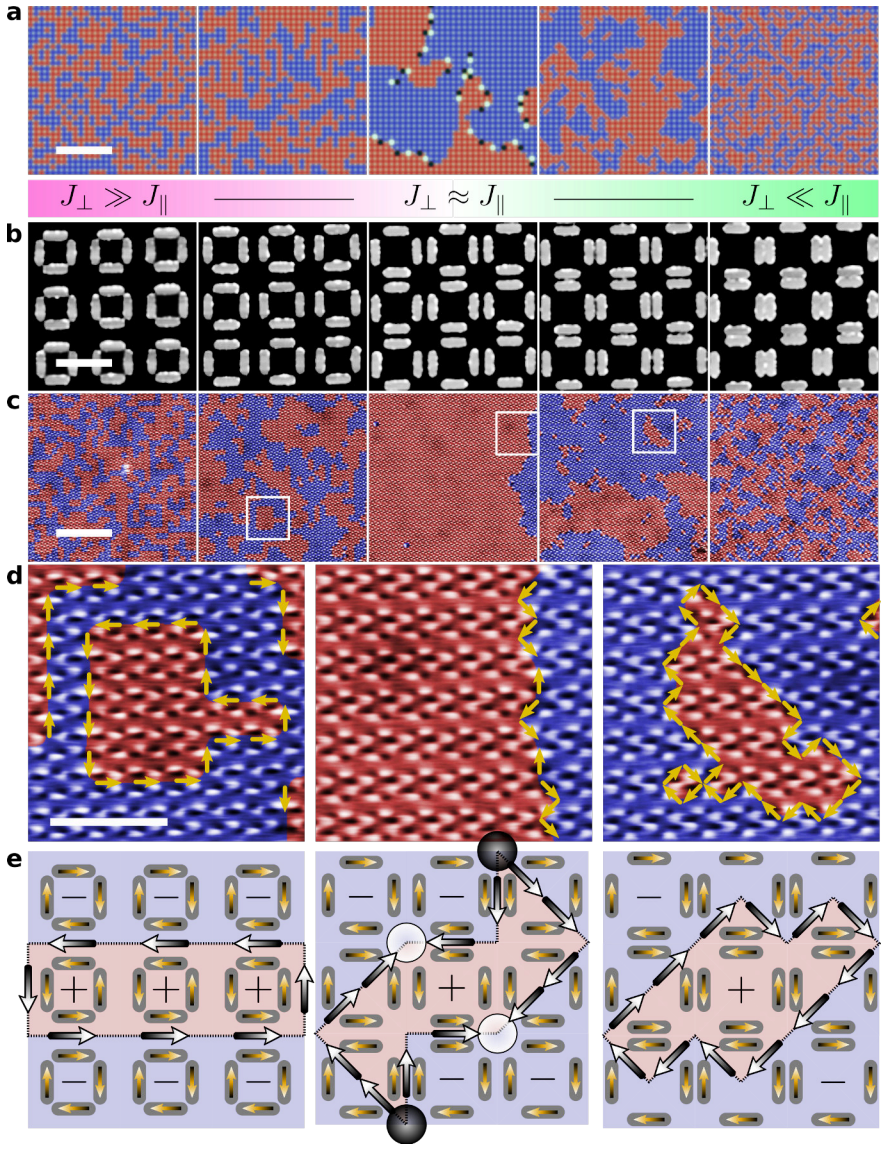

Figure 3: **Correlation between short-range order and domain formation.** **a**, MC-simulated multi-domain states obtained by a temperature quench (see Methods) for $J_\perp/J_\parallel$ = [33/1, 6/1, 1/1, 1/6, 1/33] (from left to right). Scalebar: 10 µm. **b**, Atomic-force-microscopy images of permalloy nanoarrays on silicon. The geometric variation across the series reflects the variation of $J_\perp$ and $J_\parallel$ as defined in Eqs. 5 and 6. Scalebar: 1 µm. **c**, Magnetic-force-microscopy images of the corresponding as-grown domain patterns with opposite domain states in blue and red, see Fig. 1. Scalebar: 10 µm. **d**, Magnified view of the regions outlined by white frames in (c). The local direction of magnetisation within the domain walls is shown with yellow arrows. Scalebar: 3 µm. **e**, Schematics of the domain-wall configurations for $J_\perp \gg J_\parallel$ (left), $J_\perp \approx J_\parallel$ (centre) and $J_\perp \ll J_\parallel$ (right). For $J_\perp \approx J_\parallel$, head-to-head and tail-to-tail meeting points of magnetic moments result in emergent magnetic charges (black- and white-shaded discs).

We now use the kMC-simulated multi-domain configurations to predict further relations between the microscopic coupling strength and macroscopic ferroic properties such as the density of emergent magnetic charges, which are known to affect the domain-wall mobility[2], and the associated spin-spin autocorrelation time τ (see Methods). As shown in Fig. 4, a significant number of emergent magnetic charges are obtained around $J_\perp \approx J_\parallel$. Our next step is therefore to see if, depending on $J_\perp/J_\parallel$, the path via which the system enters the ferroic phase (see Fig. 2) has an impact on the thermal domain-wall mobility, which would have direct consequences for the material's coercivity and remanence. To parametrise this domain-wall mobility, we use kMC simulations to calculate τ at $0.95\,T_\mathrm{c}$ with the result shown in Fig. 4. The corresponding spin-relaxation rate τ^{-1} closely follows the emergent-magnetic-charge density. For $J_\perp \gg J_\parallel$ and $J_\perp \ll J_\parallel$, a collective switching of the short-range-ordered octupolar or quadrupolar subunits is required. The high energy barrier for this process results in a decreased thermal mobility of the domain wall. For $J_\perp \approx J_\parallel$, however, the lack of short-range order above T_c results in comparable excitation energies for both microscopic interactions and thus in an increased density of emergent magnetic charges and a high domain-wall mobility. Hence, both spatial and temporal macroscopic measures are closely linked to the competing short-range orders so that the coupling-strength ratio can be used to control them. Note that the $J_\perp/J_\parallel$ dependencies in Fig. 4 are asymmetric with the peaks shifted towards $J_\perp < J_\parallel$. This reflects the different switching-energy barriers of the octupolar and quadrupolar subunits due to the different number of magnetic moments involved.

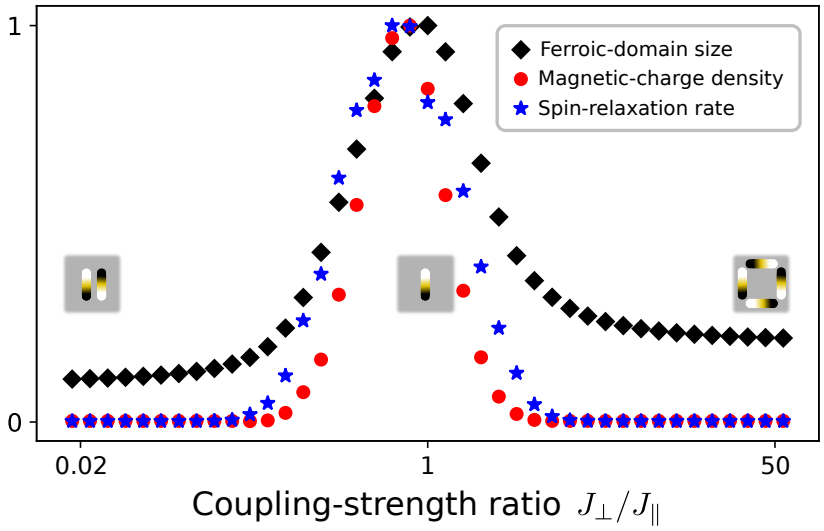

Figure 4: **Macroscopic physical properties determined by the microscopic interactions.** The average domain size (here parametrised as the mean distance between domain walls), the emergent-magnetic-charge density and the spin-relaxation rate τ^{-1} as a function of $J_\perp/J_\parallel$. All plots are normalised with respect to their maximum value. The asymmetry and shift of the peaks with respect to $J_\perp = J_\parallel$ is caused by the different energy barrier for switching the quadrupolar and octupolar short-range-ordered subunits (see text).

In conclusion, we have demonstrated, with excellent agreement between simulation and experiment, how the competition between intrinsic microscopic interactions can be used to control the macroscopic properties of a ferroic state. In our simple artificial ferroic system with compensated magnetic order, the competition of two short-range interactions determines hallmark properties of the ferroic state, such as the morphology and size of the domains, and the structure and mobility of the domain walls. Nanomagnetic arrays constitute a versatile platform to regulate the ferroic state because coupling strengths can be introduced and manipulated at will and the resulting magnetic configurations can be experimentally accessed with high spatial resolution. This important insight into the relationship between microscopic and macroscopic aspects in ordered systems with no net magnetisation is relevant given the current interest in antiferromagnetic spintronics as route towards faster and more robust digital memory as well as for neuromorphic computing[12–14].

Methods

Effective Model. For our model, we parametrise the magnetic dipole-dipole interaction in the framework of magnetic exchange interactions with the purpose to retain the link to real materials where the exchange interactions dominate the magnetic behaviour. Note that we aim here to use the simplest possible system that is sufficient to simulate ferroic order without a net magnetisation and that permits us to relate intrinsic microscopic interactions to macroscopic phenomena of ferroic states such as domain and domain-wall formation, and the associated basic physical properties. Therefore, we do not consider magnetic-dipole interactions beyond nearest-neighbours and higher-order multipole interactions because these would merely yield quantitative changes without significant qualitative differences in the results.

This leads us to the array shown in Fig. 1. For this particular design, we choose the unit cell outlined by a magenta square and define its center as the origin. From here, we identify two relevant distances: r, the distance from the center of the unit cell to the nearest nanomagnet and a, the lattice constant. We represent each nanomagnet as a point dipole $\mathbf{m}_i$ at lattice site i of equal magnetisation $m \equiv |\mathbf{m}_i|$ pointing along the long axis. The interaction energy E_D with its jth neighbouring magnetic dipole $\mathbf{m}_j$ is given by

$$E_\mathrm{D} = \frac{\mu_0}{4\pi}\left(\frac{(\mathbf{m}_i \cdot \mathbf{m}_j)}{|\mathbf{r}_{ij}|^3} - \frac{3\,(\mathbf{m}_i \cdot \mathbf{r}_{ij})(\mathbf{m}_j \cdot \mathbf{r}_{ij})}{|\mathbf{r}_{ij}|^5}\right) \quad , \tag{2}$$

where $\mathbf{r}_{ij} = \mathbf{r}_i - \mathbf{r}_j$ is the distance between dipoles at positions $\mathbf{r}_{i,j}$. We first evaluate Eqn. (2) for orthogonal nearest neighbours, where the first term becomes zero because of $\mathbf{m}_i \perp \mathbf{m}_j$. Using $\mathbf{m}_i \perp \mathbf{r}_i$ and $\mathbf{m}_i \parallel \mathbf{r}_j$ yields

$$E_\perp = \frac{3\mu_0}{4\pi|\mathbf{r}_{ij}|^5}((\mathbf{m}_i \cdot \mathbf{r}_j)(\mathbf{m}_j \cdot \mathbf{r}_i) + (\mathbf{m}_i \cdot \mathbf{r}_i)(\mathbf{m}_j \cdot \mathbf{r}_j)) \quad , \tag{3}$$

where the second product in the parenthesis is zero. By subtracting this product twice and using the Binet-Cauchy identity, Eqn. (3) can be rewritten as a vector product:

$$E_\perp = \frac{3\mu_0}{4\pi|\mathbf{r}_{ij}|^5}((\mathbf{m}_i \times \mathbf{m}_j) \cdot (\mathbf{r}_i \times \mathbf{r}_j)) \quad . \tag{4}$$

Using $|\mathbf{r}_i| = |\mathbf{r}_j| = r$, $|\mathbf{r}_{ij}| = \sqrt{2}r$, $|\mathbf{m}_i| = m$, and defining $\hat{\mathbf{D}}_{ij} = \hat{\mathbf{r}}_i \times \hat{\mathbf{r}}_j$ with $\hat{\mathbf{r}}_{i,j}$ and $\hat{\mathbf{m}}_{i,j}$ as unit vectors, gives

$$E_\perp = J_\perp\, \hat{\mathbf{D}}_{ij} \cdot (\hat{\mathbf{m}}_i \times \hat{\mathbf{m}}_j) \quad \text{with} \quad J_\perp \equiv \frac{3\mu_0 m^2}{16\pi\sqrt{2}r^3} \quad , \tag{5}$$

which is mathematically equivalent to an antisymmetric exchange interaction with $J_\perp$ as the coupling strength.

For the case of parallel nearest neighbours, the second term in E_{D} becomes zero because $\mathbf{m}_i \perp \mathbf{r}_{ij}$. Using $|\mathbf{r}_{ij}| = 2(a-r) \equiv d$ yields

$$E_{\parallel} = J_{\parallel}\, \hat{\mathbf{m}}_i \cdot \hat{\mathbf{m}}_j \quad \text{with} \quad J_{\parallel} \equiv \frac{\mu_0 m^2}{4\pi d^3} \quad , \tag{6}$$

which is mathematically equivalent to a symmetric exchange interaction with $J_{\parallel}$ as the coupling strength.

Hence, the two coupling constants $(J_{\perp}, J_{\parallel})$, whose competition determines the physical properties of the ferroic system, are each represented by one of the two geometric units (r, d) parametrising the structure of the system.

Monte-Carlo simulations. We use a lattice of $N = 100 \times 100$ unit cells with periodic boundary conditions and represent the magnetisation of each nanomagnet as a bidirectional classical spin, coupled to its neighbours with interaction strengths $J_{\perp}$ and $J_{\parallel}$, as detailed above. We define temperature in units of the coupling strengths and therefore set $k_B = 1$. We tune $J_{\perp}$ and $J_{\parallel}$ while keeping the sum $J_{\perp} + J_{\parallel}$ constant, which we achieve by setting

$$J_{\perp} = J_0(1 - \tanh(\delta)) \quad \text{and} \tag{7}$$

$$J_{\parallel} = J_0(1 + \tanh(\delta)) \quad , \tag{8}$$

where the amplitude J_0 represents an arbitrary scaling factor and and δ determines the ratio between the interactions. Choosing $J_0 = 50$ and $\delta \in \{-2.0, -1.9, .., 1.9, 2.0\}$ we obtain the 41 coupling strengths used in Fig. 2, which cover all three different pathways to the ground state (see main text). In order to distinguish between the three pathways, we introduce the octupole population density O and the quadrupole population density Q as follows

$$O = \langle\, \frac{1}{4N} \sum_{u=1}^{N} |\sum_{j=1}^{4} \hat{\mathbf{r}}_j \times \hat{\mathbf{m}}_{u,j}| \,\rangle \quad \text{and} \tag{9}$$

$$Q = \langle\, \frac{1}{16N} \sum_{u=1}^{N} \sum_{j=1}^{4} |\hat{\mathbf{m}}_{u,j} - \hat{\mathbf{m}}^{\parallel}_{u,j}| \,\rangle \quad , \tag{10}$$

where $\langle ... \rangle$ indicates the statistical average, $\mathbf{r}_j$ denotes the position vector of the j-th nanomagnet within a unit cell, while the index u runs over all unit cells. Furthermore, $\mathbf{m}^{\parallel}_{u,j}$ indicates the magnetisation of the parallel nearest neighbour within the adjacent unit cell of the nanomagnet $\mathbf{m}_{u,j}$. The amplitude of the order parameter of the system[16] is defined as

$$\mathcal{T} = \langle\, \frac{1}{4N} |\sum_{u=1}^{N} \sum_{j=1}^{4} \hat{\mathbf{r}}_j \times \hat{\mathbf{m}}_{u,j}| \,\rangle \quad . \tag{11}$$

The equilibrium MC simulations displayed in Fig. 2 are obtained using the Metropolis algorithm with simulated annealing. For each ratio of $J_\perp/J_\parallel$, we start at $T = 4J_0$ and decrease the temperature as described below. At each temperature, we perform 10^3 Metropolis sweeps to reach thermal equilibrium, and then perform another 10^4 sweeps to average the observables Q, O and $\mathcal{T}$. We calculate the specific heat C_v and decrease the temperature in steps of $\Delta T = 2 \cdot T/\sqrt{C_v}$, which allows us to increase the density of data points where the observables vary most. We repeat this procedure until we reach the ground state characterised by $\mathcal{T} = 1$. The four-spin octupolar and two-spin quadrupolar subunits at $J_\perp \gg J_\parallel$ and $J_\perp \ll J_\parallel$, respectively, cost significant energy to break up, so that we introduce collective flips of the magnetisation of these subunits into our simulation. This allows the system to efficiently find its ground state with decreasing temperature.

All out-of-equilibrium simulations (Fig. 3a and Fig. 4) are performed using a kinetic Monte-Carlo (kMC) algorithm with the so-called n-fold way introduced by Bortz, Karlos and Lebowitz[34]. When generating the multi-domain patterns shown in Fig. 3a, we start at $T = 4J_0$ and rapidly decrease the temperature below T_c in order to prevent the system from reaching equilibrium. We extract the resulting domain configuration, the emergent-magnetic-charge density and the average distance between domain walls with the results shown in Fig. 4, where all quantities are averaged over 10^3 independent runs. To calculate the autocorrelation time τ, defined as

$$\tau = \int_0^\infty \frac{G(t)}{G(0)} dt \quad , \tag{12}$$

we create an equilibrium state at $0.95\,T_\mathrm{c}$. This relative temperature, in contrast to an absolute temperature, results in a comparable thermal excitation for all systems. We use kMC to allow this equilibrium state to evolve and calculate the spin-autocorrelation function $G(t) = \langle\, \hat{\mathbf{m}}_i(0) \cdot \hat{\mathbf{m}}_i(t) \,\rangle$. We extract $G(t)$ after each time step and determine its average over the entire system. Finally, we determine the average of τ over 100 runs.

Sample fabrication. Using electron-beam lithography, the different two-dimensional arrays of nanomagnets were patterned on a single silicon-(100) substrate. Subsequently, a 12-nm-thick permalloy ($Ni_{81}Fe_{19}$) film was deposited simultaneously on all patterns by electron-beam evaporation with a growth rate of 3 Å/min and capped with a 4-nm-thick film of gold to prevent oxidation. Finally, unwanted material was removed in an ultrasonic-assisted lift-off process. All patterned arrays measure $55 \times 55\,\mu\mathrm{m}^2$. Four stadium-shaped nanomagnets with lateral dimensions $450 \times 150\,\mathrm{nm}^2$ form the artificial unit cell of our square lattice with $a = 1\,\mu\mathrm{m}$ lattice period, see Fig. 1. The nanomagnet aspect ratio of 3:1 and the choice of permalloy as a soft magnetic material ensure the formation of single-domain macrospins with magnetic moments pointing parallel (or antiparallel) to the nanomagnet's long edge. To tune the strength of the pairwise interactions

$J_\perp$ and $J_\parallel$, the structural parameter r is modified to vary the spacing between parallel neighbouring nanomagnets from 32 nm up to 257 nm and, accordingly, between perpendicular neighbouring magnets from 216 nm down to 57 nm.

Micromagnetic imaging. Magnetic imaging was performed using an NT-MDT NTEGRA magnetic force microscope in semi-contact mode with a lift height of 45 nm. We probed the magnetic configurations by scanning the nanomagnetic arrays with a Nanosensors PPP-LM-MFMR magnetic tip. Raster scans with a 10 µm/s tip velocity along the fast axis and line-to-line spacings of 30 nm were applied for scanning areas of $30 \times 30\,\mu m^2$ within the array.

References

1. Wadhawan, V. K. *Introduction to ferroic materials* (CRC Press, 2000).

2. Hubert, A. & Schaefer, R. *Magnetic domains: the analysis of magnetic microstructures* (Springer, 2009).

3. Seul, M. & Andelman, D. Domain shapes and patterns: The phenomenology of modulated phases. *Science* **267**, 476–483 (1995).

4. Farztdinov, M. M. Structure of antiferromagnets. *Soviet Physics Uspekhi* **7**, 855–876 (1965).

5. Fiebig, M., Froehlich, D., Leute, S. & Pisarev, R. V. Second harmonic spectroscopy and control of domain size in antiferromagnetic $YMnO_3$. *Journal of Applied Physics* **83**, 6560–6562 (1998).

6. Nisoli, C., Moessner, R. & Schiffer, P. *Colloquium*: Artificial spin ice: designing and imaging magnetic frustration. *Reviews of Modern Physics* **85**, 1473–1490 (2013).

7. Heyderman, L. J. & Stamps, R. L. Artificial ferroic systems: novel functionality from structure, interactions and dynamics. *Journal of Physics: Condensed Matter* **25**, 363201 (2013).

8. Rougemaille, N. & Canals, B. Cooperative magnetic phenomena in artificial spin systems: spin liquids, Coulomb phase and fragmentation of magnetism – a colloquium. *The European Physical Journal B* **92**, 62 (2019).

9. Skjaervo, S. H., Marrows, C. H., Stamps, R. L. & Heyderman, L. J. Advances in artificial spin ice. *Nature Reviews Physics* **2**, 13–28 (2020).

10. Kittel, C. Physical theory of ferromagnetic domains. *Reviews of Modern Physics* **21**, 541–583 (1949).

11. Sander, D. *et al.* The 2017 magnetism roadmap. *Journal of Physics D: Applied Physics* **50**, 363001 (2017).

12. Jungwirth, T. *et al.* The multiple directions of antiferromagnetic spintronics. *Nature Physics* **14**, 200–203 (2018).

13. Jungwirth, T., Marti, X., Wadley, P. & Wunderlich, J. Antiferromagnetic spintronics. *Nature Nanotechnology* **11**, 231–241 (2016).

14. Wadley, P. *et al.* Electrical switching of an antiferromagnet. *Science* **351**, 587–590 (2016).

15. Gomonay, H. V. & Loktev, V. M. Shape-induced phenomena in finite-size antiferromagnets. *Physical Review B* **75**, 174439 (2007).

16. Lehmann, J., Donnelly, C., Derlet, P. M., Heyderman, L. J. & Fiebig, M. Poling of an artificial magneto-toroidal crystal. *Nature Nanotechnology* **14**, 141–144 (2019).

17. Luttinger, J. M. & Tisza, L. Theory of dipole interaction in crystals. *Physical Review* **70**, 954–964 (1946).

18. Kraemer, C. *et al.* Dipolar antiferromagnetism and quantum criticality in $LiErF_4$. *Science* **336**, 1416–1419 (2012).

19. Alkadour, B., Mercer, J. I., Whitehead, J. P., Southern, B. W. & van Lierop, J. Dipolar ferromagnetism in three-dimensional superlattices of nanoparticles. *Physical Review B* **95**, 214407 (2017).

20. Sendetskyi, O. *et al.* Continuous magnetic phase transition in artificial square ice. *Physical Review B* **99**, 214430 (2019).

21. Wang, R. F. *et al.* Artificial 'spin ice' in a geometrically frustrated lattice of nanoscale ferromagnetic islands. *Nature* **439**, 303–306 (2006).

22. Ladak, S., Read, D. E., Perkins, G. K., Cohen, L. F. & Branford, W. R. Direct observation of magnetic monopole defects in an artificial spin-ice system. *Nature Physics* **6**, 359–363 (2010).

23. Mengotti, E. *et al.* Real-space observation of emergent magnetic monopoles and associated dirac strings in artificial kagome spin ice. *Nature Physics* **7**, 68–74 (2011).

24. Farhan, A. *et al.* Exploring hyper-cubic energy landscapes in thermally active finite artificial spin-ice systems. *Nature Physics* **9**, 375–382 (2013).

25. Kapaklis, V. *et al.* Thermal fluctuations in artificial spin ice. *Nature Nanotechnology* **9**, 514–519 (2014).

26. Anghinolfi, L. *et al.* Thermodynamic phase transitions in a frustrated magnetic metamaterial. *Nature Communications* **6**, 8278 (2015).

27. Farhan, A. *et al.* Direct observation of thermal relaxation in artificial spin ice. *Physical Review Letters* **111**, 057204 (2013).

28. Gliga, S. *et al.* Emergent dynamic chirality in a thermally driven artificial spin ratchet. *Nature Materials* **16**, 1106–1111 (2017).

29. Loreto, R. P. *et al.* Emergence and mobility of monopoles in a unidirectional arrangement of magnetic nanoislands. *Nanotechnology* **26**, 295303 (2015).

30. Arnalds, U. B. *et al.* A new look on the two-dimensional Ising model: thermal artificial spins. *New Journal of Physics* **18**, 023008 (2016).

31. Morgan, J. P., Stein, A., Langridge, S. & Marrows, C. H. Thermal ground-state ordering and elementary excitations in artificial magnetic square ice. *Nature Physics* **7**, 75–79 (2011).

32. Nisoli, C. On thermalization of magnetic nano-arrays at fabrication. *New Journal of Physics* **14**, 035017 (2012).

33. Mol, L. A. *et al.* Magnetic monopole and string excitations in two-dimensional spin ice. *Journal of Applied Physics* **106**, 063913 (2009).

34. Bortz, A., Kalos, M. & Lebowitz, J. A new algorithm for Monte Carlo simulation of Ising spin systems. *Journal of Computational Physics* **17**, 10 – 18 (1975).

Data availability The data that support the Figures and other findings of this study can be found here (doi:10.3929/ethz-b-000429489).

Code availability The program codes that support the Figures and other findings of this study can be found here (doi:10.3929/ethz-b-000429490). Additional data and information is available from the corresponding authors upon reasonable request.

Acknowledgement We thank Thomas Lottermoser, Saül Vélez Centoral, Andres Cano and Thomas Weber for discussions. M.F. acknowledges funding by the Swiss National Science Foundation (Project No. 200021-175926). J.L. and M.F. acknowledge funding by the ETH Research Grant No. ETH-28 14-1 "Resonant optical magnetoelectric effect in magnetic nanostructures". A.B. and M.F. acknowledge funding by the European Research Council (Advanced Grant No. 694955 – INSEETO). N.L. and L.J.H. acknowledge funding by the Swiss National Science Foundation (Project No. 200021-155917).

Author contribution All authors contributed to the discussion and interpretation of the study. J.L., A.B. and M.F. wrote the manuscript with input from all co-authors. C.D. and N.L. fabricated the nanomagnetic structures. J.L. performed magnetic force microscopy experiments. A.B. and P.M.D. performed the Monte-Carlo simulations. M.F. and L.J.H. supervised the study.

Competing Interests The authors declare that they have no competing financial interests.

Additional Information

Correspondence and requests for materials should be addressed to J.L., A.B., or M.F.

Reprints and permissions information is available at www.nature.com/reprints.